Design and testing of advanced liquid metal targets for DEMO divertor: The OLMAT project

D. Alegre*, E. Oyarzabal, D. Tafalla, M. Liniers, A. Soleto and F. L. Tabarés

Laboratorio Nacional Fusion. CIEMAT. Av Complutense 40. 28040 Madrid. Spain

*Corresponding author: daniel.alegre@ciemat.es

ORCID

D. Alegre: 0000-0002-1665-7811

Keywords: liquid metals, divertor simulator, vapor shielding, redeposition, DEMO, CPS

Abstract

In a future fusion reactor like DEMO (DEMOnstration reactor) one of the main concerns is the handling of the power exhaust from the plasma, especially at the divertor. The expected power loads cannot easily be handled by traditional armor solutions based on solid materials like tungsten, especially when the effect of intense neutron bombardment is also considered. Interest in armor concepts based on liquid metals has been subsequently on the rise, as they prove to be more resilient against high, fast power loads and neutron bombardment. However, engineering solutions for those concepts are very complex, and need to be tested. For this purpose, OLMAT project (Optimization of Liquid Metal Advanced Targets) has been envisaged. The project will use the NBI (Neutral Beam Injection) of the TJ-II stellarator to irradiate liquid metal targets with power densities (neutrals plus occasionally ions) relevant to DEMO steady state operation, in the range of 20 MW/m^2. OLMAT design will allow a series of experiments that other divertor simulator devices cannot easily perform: in-situ measurements of hydrogen retention, redeposition, vapor shielding, material fatigue, dust and precipitates effects, etc. Moreover, a high-power fiber laser will be used to simulate ELMs (Edge Localized Modes) in a small area, or to simulate the strike point power deposition profile.

1. Introduction

Materials resilience is one the main causes of the delay in the achievement of an economically viable nuclear fusion reactor based on magnetic confinement. This is especially true for the inner shielding at the divertor area against the plasma exhaust (i.e. strike points): the target plates. Peak power densities up to 20 MW/m^2 may arise during normal operation [1]. Moreover, off-normal transient events like ELMs, disruptions and VDEs (Vertical Displacement Events), if not mitigated, may lead to fast (1 ms) power loads ranging from a few GW/m^2 (ELMs) to tens GW/m^2 (disruptions and VDEs), see [1] and references therein. When the critical damage caused by intense neutron bombardment is also considered, the resilience of traditional shielding based on solid materials like tungsten, or even advanced materials like tungsten fibers, is seriously compromised [1,2]. Opposed to this, liquid metals (LM) offer conceptual advantages such as the lack of permanent damage and the possibility of in-situ replacement, among others [3,4].

LM-based armors are underdeveloped compared to solid-based armors [3,4] and important physics and engineering problems need to be overcome. The physics challenges related to liquid metals inside a DEMO-type reactor include melt splashing during transients and liquid displacement by jxB forces, among others [5,6]. In order to solve them, different strategies are being followed. In USA and China thermoelectric currents and/or high LM velocities have been used to stabilize the LM [7–10]. In Europe the research has been focused on Capillary Porous Systems (CPS), initially developed in Russia [3–5,11–20]. In CPS the liquid metal is bonded to the surface by capillary forces. They have shown promising results in the suppression of LM instabilities [3–5,11–15], and a good performance in divertor simulator devices against high-load transients like disruptions and type-I ELMS (see [12,19,20] and references therein).

Eurofusion has recently acknowledged the LM armor as an alternative to the W-based armor of DEMO divertor [21]. Furthermore, the pre-conceptual design has been very recently approved in a gate review [22]. Mock-ups based on CPS technology must be built and tested in devices that simulate the conditions in DEMO. In order to achieve this, the OLMAT project (Optimization of Liquid Metal Advanced Targets in TJ-II) is being developed at CIEMAT. It is based on the use of the Neutral Beam Injectors (NBI) of the TJ-II stellarator for the irradiation of LM targets (mainly CPS) at DEMO-relevant powers. The characteristics of the NBI beam are adequate for the simulation of steady state and slow transient powers (10-20 MW/m^2) including vapor shielding and fatigue studies. Moreover, the NBI beam is wide enough to irradiate large samples (~20 cm diameter), allowing redeposition studies of the eroded and evaporated material. In a second stage of the project a Continuous Wave (CW), high-power fiber laser will be used to simulate ELM-like powers in a small area, or the strike point power deposition profile. Although integrated in the NBI duct line, OLMAT will routinely operate isolated from TJ-II. The OLMAT chamber has been designed so that TJ-II walls are largely shielded from LM deposition. Therefore, contrary to other devices, no deleterious impact of OLMAT operation on the TJ-II performance is expected. TJ-II has been routinely operated with lithium coating and run experiments with LM limiters. Even after experimental campaigns with Sn and SnLi (where significant amounts of Sn were deposited inside TJ-II chamber), no irreversible adverse effects have been observed in TJ-II plasmas.

An overview of the OLMAT project, including the TJ-II stellarator adaptation, the three project phases, NBI beam characteristics, and the planned upgrades will be given in section 2. The experiments that can be performed within the OLMAT project, highlighting the ones no other device can achieve, will be sketched in section 3. Finally, in section 4 the advantages and limitations of the OLMAT project will be presented.

2. The OLMAT project

The project will be deployed in three phases. Briefly:

- Phase I: The TJ-II NBI system will be modified to allow insertion of the LM target in the beam path. Pulsed irradiations of 150 ms with close to 20 MW/m^2 power (optionally up to 27 MW/m^2) and a 2 min repetition rate will be carried out.

- Phase II: during this phase a high-power CW laser will be added for ELM-like high power local irradiation or strike point area simulation.

- Phase III: the upgrade of one of the TJ-II NBI injectors to allow long pulse irradiation of the target (5 s).

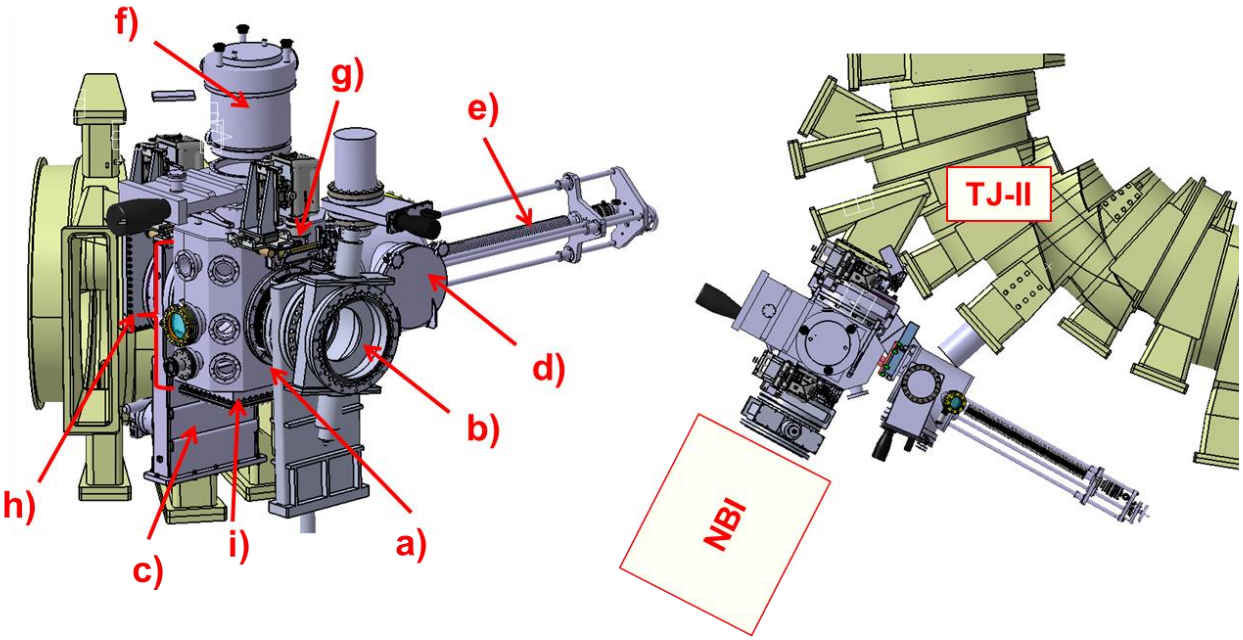

Fig.*1 CAD design of OLMAT. Lateral view (left) and upper view (right) a) irradiation chamber; b) gate valve to NBI; c) gate valve to TJ-II; d) pre-chamber for sample loading; e) sample insertion system; f) upper turbopump with liquid metal condensation bafflers; g) BaF_2 optical window for infrared thermography; h) diagnostic ports and windows; i) lower port for LMD prototype testing.*

2.1 TJ-II adaptation for OLMAT

The OLMAT project will use the TJ-II Counter-NBI injector to irradiate LM targets. The irradiation chamber will be located at the NBI duct, which will be modified to accommodate the new experiment, see Figure 1 right. As can be seen in Figure 1 left, the OLMAT irradiation chamber can be isolated from both the TJ-II main chamber and the NBI system by means of two gate valves. During target irradiation, the OLMAT chamber will usually be isolated from TJ-II by the gate valve c), although it may be connected to TJ-II vacuum when this valve is kept open. In this case, insertion of a beam stop plate at the end of the NBI duct will ensure a low gas conductance and shielding of TJ-II walls from metal vapor deposition. The chamber will be directly pumped by a separate set of mechanical pumps (turbopump in series with a rough pump) to allow independent operation from TJ-II, and minimize influence on TJ-II plasmas. This configuration will allow OLMAT experiments (without plasma/magnetic field) to be run with reduced operational costs and be easily alternated with standard TJ-II plasma campaigns.

As can be seen in Figure 1 left, the OLMAT irradiation chamber is equipped with a large number of windows and ports to allow for currently available diagnostics (infrared thermography —IR— with BaF_2 windows, Optical Emission Spectroscopy —OES—, visible cameras, etc.) as well as future upgrades like the high-power CW laser in Phase II. The pre-chamber is necessary to load the target with the sample holder while preserving low contamination levels in the irradiation chamber. In the

pre-chamber the sample will be loaded horizontally to ease its manipulation and the initial melting of the liquid metal. When ready for operation, the target will be rotated to a vertical plane and displaced horizontally for insertion in the irradiation chamber, with the help of the manipulator. With the present design the size of the target in the pre-chamber is limited to 25 cm in diameter and 4 cm thickness.

Finally, at the bottom of the irradiation chamber (part *i* of Figure 1 left) a large port is placed to insert large CPS prototypes. Since no independent pumping is possible in this location its use will be limited in order to minimize the contamination in the irradiation chamber.

2.2 NBI beam characteristics

The TJ-II NBI characteristics are described in Table 1. The H^0 beam energy (<35 keV) was chosen to optimize beam absorption in a typical TJ-II plasma. The three energy species —E_0, $E_0/2$, $E_0/3$— originating as molecular ions in the ion source, account respectively for 50%, 25% and 25% of the beam particles. Beam transmission into TJ-II has been carefully studied by means of the 3D geometric code DENSB [23]. With the present design of drift duct the overall geometric transmission including the first toroidal field coil is around 62%, which gives a calculated power into the torus of 700 kW. This low transmission is caused by a thick water-cooled copper diaphragm of 20 cm diameter placed as front duct piece to limit thermal loads in the TJ-II beam-entrance area while minimizing the reionization losses and the gas load into the TJ-II chamber. The injected power can be increased by 35% if the Magnetic Deflector of the residual ion dump is suppressed. This situation is undesirable for regular TJ-II plasma operation but may be interesting in OLMAT. In this case a mix of high energy neutrals and ions will impact on the target creating a highly radiative plasma, thus allowing more realistic studies of vapor shielding (see details in section 3.4).

Table 1: NBI parameters of TJ-II stellarator

Working gas	H_2
Acceleration voltage	25-35 keV
Energy species mix (E_0:$E_0/2$:$E_0/3$)	50:25:25
Acceleration current	40-60 A
Pulse length	150 ms
Repetition rate	~2 min
Gas throughput	20 Torr.l.s^{-1}

At the target, located close to the focal plane, the neutral beams have a Gaussian profile with a 1/e width that varies around 20 cm depending on beam parameters. The effect of the copper diaphragm (1 meter upstream of the target) is to decrease the power on the beam periphery while leaving the central region unchanged, as can be seen in Figure 2, which depicts DENSB profile simulations of a typical beam with and without copper diaphragm. The beam width is significantly larger than interaction areas at usual plasma simulator devices, which usually are in the order of a few cm. This unique characteristic allows more realistic plasma loads, especially in terms of re-deposition, as will be explained in section 3.3. Moreover, the acceleration voltage and current may be controlled, see

Table 1 and Figure 3, to allow for different power deposition profiles. Beam characterization is carried out by means of infrared thermography of a target calorimeter. The thermal print of the beam on a textured graphite plate is analyzed, to yield the beam power density profiles [24]. Figure 3a shows the profiles corresponding to a beam current (I_{accel}) scan at fixed acceleration voltage (V_{accel}), and Figure 3b a beam energy scan (V_{accel}) at fixed beam current (I_{accel}). Not only lower power densities but also flatter profiles may be generated. As can be seen in Figure 3 the acceleration voltage scan allows the peak power density to be varied between ~7 MW/m^2, with a nearly flat profile, and ~19 MW/m^2 with a narrower profile.

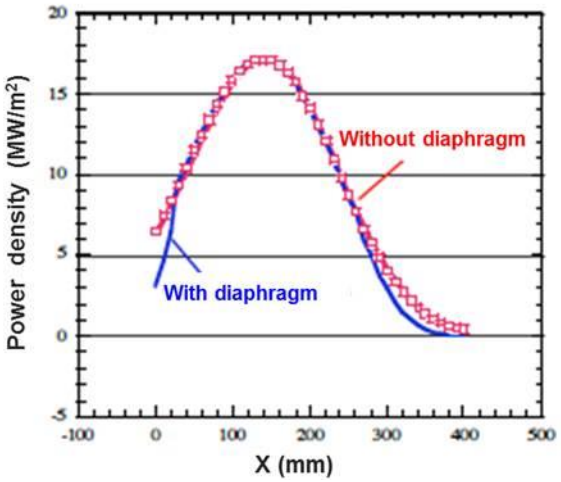

Fig. 2: *DENSB simulation of the power density profile on a vertical plane near the beam focus. The effect of the 20 cm diameter copper diaphragm is shown.*

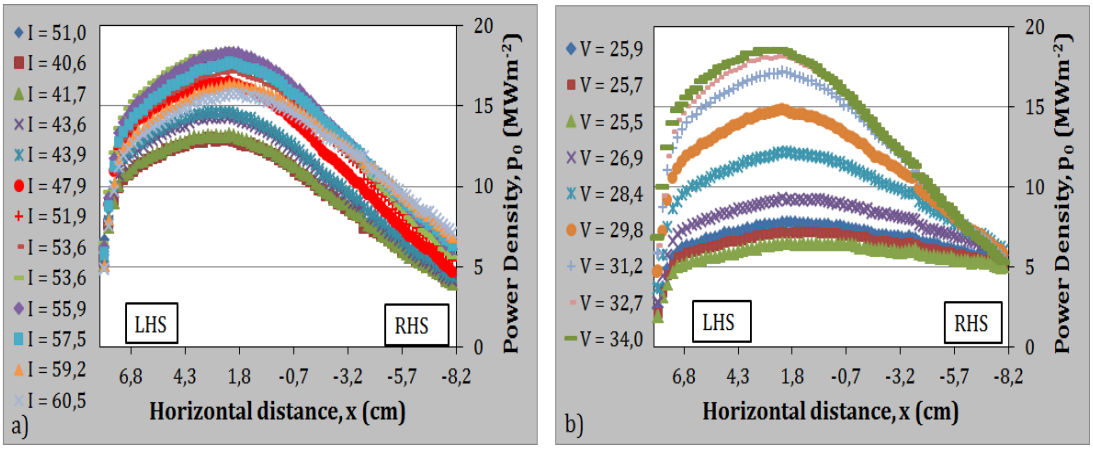

Fig. 3: *Power density measured by infrared thermography. a) scan in acceleration current at 31.5 keV acceleration voltage; b) scan in acceleration voltage at 53 A of acceleration current.*

Beam characteristics at the target region are summarized in Table 2. The effect of the high energy beam particles in the OLMAT experiment must be compared with the low-temperature high-density plasma at the DEMO divertor. The energy of the OLMAT beam particles is in the order of tens of

keV while in DEMO divertor they will be around 10-20 eV in steady state and tens of keV for ELMs [1]. Particle fluxes are 2-3 orders of magnitude lower in OLMAT than in DEMO [1]. However, due to the nature of liquid metals (liquid film mobility), and being the thickness of the liquid layer (about 100 μm [12]) much larger than the power deposition range (tens of nm for steady state DEMO and <1 μm estimated for the OLMAT beam [25]), the intense power deposition on the LM target of OLMAT will yield results relevant to DEMO. The extrapolation of some specific effects to DEMO will need complementary approaches, as it is the case in other kinds of divertor plasma simulators [26].

Table 2: NBI beam characteristics at the target region

Power	0.7 MW
Power density	7-20 MW/m^2
Main particle energy (E_0)	25-35 keV
Particle flux	4-5·10^{21} m^{-2}s^{-1}
Gaussian 1/e width	20 cm
Local pressure	10-20(25) Pa

With the present NBI system, the pulse length is limited to ~ 150 ms, but a high repetition rate, 2 minutes between pulses, is possible. This results in an accumulated exposure time of 30-35 s or around 200-250 pulses per day. Fatigue studies, of paramount importance for mitigated ELMs and DEMO scenarios working in short (hours) pulses are therefore feasible (see section 3.5). On the other hand, the time response simulations carried out by Vertkov et al for the CPS system at the Liquid Lithium Limiters of TJ-II [27], can be used to estimate the temperature increase of the CPS in OLMAT. Only heat conduction from the surface to the limiter body was assumed in the calculation (inertial cooling). Two materials were considered for the CPS mesh, W and stainless steel. The results for several values of the incident power are shown at Figure 4. In the absence of any other heat dissipation mechanism (vapor shielding, evaporation, convection…) an increase in the CPS surface temperature of near 550 ºC is achieved at the end of the NBI pulse (~150 ms) for a tungsten mesh at 10 MW/m^2 incident power. An insight on the heat dissipation mechanisms present at OLMAT may be obtained by comparison of the experimentally observed thermal behavior with computer simulations of the temperature increase under different dissipation scenarios.

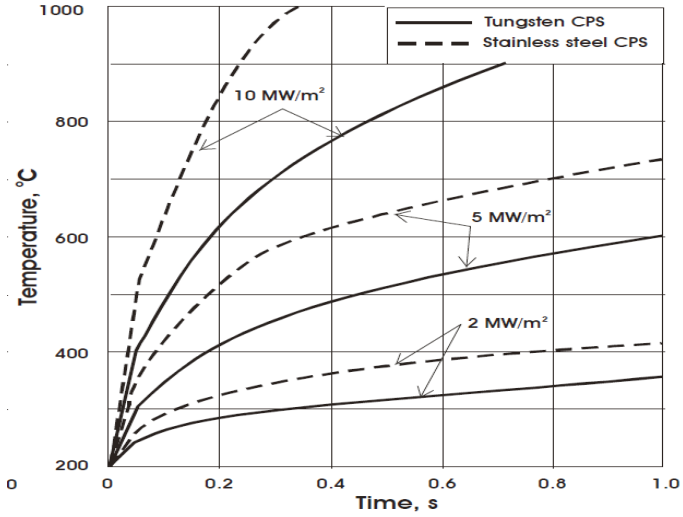

***Fig.** 4: Temperature excursion during the exposure of a CPS Liquid Lithium Limiter (TJ-II) to short heat pulses*

In Table 2, the estimated range of attainable pressure values in front of the target is given. Within this range of pressure, the experiments may yield meaningful results in vapor shielding and liquid metal splashing studies. This sets OLMAT in a position of advantage with respect to other devices, such as Quasi-Stationary Plasma Accelerators (QSPA), with much higher pressure values [26]. In the pressure estimates, only the momentum transfer of the fast incident particles is taken into account. The contribution of the gas cloud originated from recycling of the fast particles can be disregarded, since, even assuming a recycling coefficient of one, the resulting gas pressure is three orders of magnitude lower than the fast particle contribution.

In the pressure equation full momentum transfer to the target is assumed:

$$P = \frac{1}{A} \cdot m \cdot v \cdot \Gamma$$

A is the beam area, taken as the Gaussian 1/e beam width; m is the beam particle mass (H^0); v is the velocity of the incident particles; and Γ is the fast particle flux. The contribution to the pressure of the energy species mix given in Table 1 (i.e. E_0, $E_0/2$, $E_0/3$ has been considered).

Writing the fast particle energy as a function of the acceleration voltage (in Volts), and the fast particle flux as the transmitted fraction of the acceleration current (in Amperes), the pressure in front of the target takes the form:

$$P = 1.7 \cdot 10^{-3} \cdot I_{accel} \cdot \sqrt{V_{accel}}$$

where an overall beam transmission factor of 0.34 from the Ion Source to the target is considered (neutralization and transmission factors).

As can be seen in Table 2, during normal operation of OLMAT a range of pressures of ~10-20 Pa may be reached. A maximum of ~25 Pa may be attained if the Magnetic Deflector of the NBI is suppressed and both neutral and charged particles from the beam hit the target.

2.3 CW laser characteristics

A high power, CW fiber laser is being purchased for OLMAT project. Its general characteristics are highly flexible: continuous wave mode; or a pulse mode with duration from 0.1 to few ms, easily variable power, up to 150-200 J energy, 5-20 kW power (a few GW/m^2 for 10 mm^2 laser spot) and a pulse frequency of a few kHz. In this way, DEMO Type I ELMs —1-10 Hz and 0.5-1 GW/m^2 power— and DEMO Type III ELMs —difficult to predict, but few kHz and few MW/m^2 power expected— may be simulated.

The laser may also be used in continuous wave with the spot expanded in a long ellipse by a set of actively cooled cylindrical lenses. In this way, an ellipse of 0.5-1 mm height by tens of mm wide and a power density of 10-20 MW/m^2 may be obtained. This ellipsoid laser spot may be used to simulate the thin and worst-case strike point predicted for DEMO [28] under continuous heating conditions.

2.4 PINI source upgrade

In order to achieve long pulse operation during the Phase III of OLMAT a replacement of the ion source of the NBI is mandatory. This upgrade would allow to reach steady state conditions (> 5 s) at higher power density values.

The preferred option is a PINI (Positive Ion Neutral Injector) ion source. This technology is well established and is currently used in the NBI systems at the main nuclear fusion devices [29] (JET, MAST, AUG, W7X, DIIID, etc.). This PINI Ion Source would operate at 40 kV acceleration voltage and 80 A ion current, which would give a neutral beam power in excess of 1 MW in the TJ-II torus. The power density at the target is expected to be higher than 30 MW/m^2, due to the low beam divergence obtainable with the PINI grid design. On the other hand, due to the larger power (from 0.7 to 1 MW) and longer pulse length (from 150 ms to >5 s), an upgrade of the power handling systems (Ion Dump, V-Calorimeter, Duct scrapers) must be undertaken. Active cooling of the target and beam dump will be implemented for this scenario.

3. Experimental program

The experiments that may be performed in OLMAT will be now sketched. A more detailed description is given only where other devices have performance limitations, from 3.3 onwards.

3.1 CPS optimization experiments

10 cm diameter targets will initially be used, as in Figure 5. The target consists of two parts, a crucible and a cap —both made of TZM (Mo alloy) to avoid Sn corrosion— used to hold in place the porous structure (sample) of 7 cm diameter. Samples will usually be made of Tungsten wire mesh, but laser-micro-textured sheets or 3D-printed sheets will also be tested. A wire heater in a flat spiral at the back of the plate will enable to reach temperatures near ~800 K in the liquid metal.

In Phase I the resilience of CPS samples, with different porous structures and liquid metals (Li, Sn and LiSn), will be tested against DEMO slow transients, 10 and 20 MW/m^2. A comparison of the different structures will be made with the aim to find an optimal compromise between refilling time (larger pores) and instabilities suppression (smaller pores) [3]. Any substrate damage will be detected in situ looking at its emission lines (usually W) by means of OES. The IR thermography

will allow an estimation of the evaporation of the liquid metal and the heat handling capacity of the CPS [30].

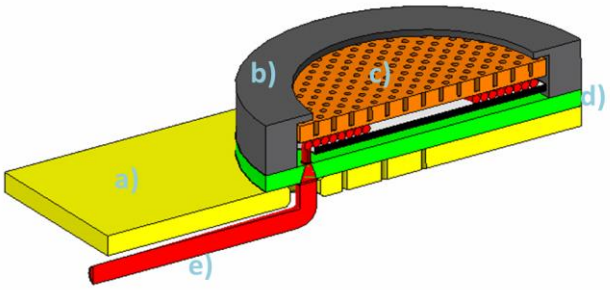

Fig.5 *OLMAT target. a) target holder; b) cap; c) crucible; d) insulation e) heater*

In Phase II the resilience of CPS samples against the synergistic combination of DEMO slow transients with ELM thermal loads by the CW laser will be done. Issues such as surface replenishment between ELMS, defined by liquid metal refilling time, and droplet ejection are paramount. While the first point will be directly determined by the chosen CPS geometry and operating temperature, local plasma pressure plays a critical role in the splashing of molten materials (as estimated in section 2.2). LIBS (Laser-Induced Breakdown Spectroscopy) may also be used to study directly the refilling time of the CPS samples. Moreover, local damage to the porous structure may be caused on purpose to check the liquid metal capacity to protect the sample.

The steady state reached in Phase III would allow more realistic tests, especially in large prototypes. Comparison with thermal load simulations will be easier too.

3.2 H content and hydride formation

Reaction of liquid metals with fuel is a main concern [2,3,11,14]. This is especially true for Lithium. In order to keep the tritium retention under control in a reactor the Li temperature must be above ~750-800 K (tritium only in solution), while the expected low pressure at DEMO divertor — 10-20 Pa near the strike points, and a few Pa over the rest of the divertor [31,32]— will hamper the generation of LiT [11]. The operational window for Lithium is further limited to 750-900 K to avoid excessive evaporation. Nevertheless, at some locations far from the strike points where the lithium will be cooler, metal hydrides may form.

Recent experiments [33] have shown that the tritium retention in tin is as low as in tungsten. Notwithstanding, stannane generation has been detected in different experiments at low and DEMO-relevant hydrogen fluxes [14]. Although its decomposition in the plasma and at the walls will be fast and no tritium codeposits are expected, stannane formation will lead to enhanced erosion and redeposition of tin in plasma-shadowed surfaces, which may be a concern for dust generation.

Experiments in both phases I and III (steady state) will be aimed to study the accumulated H retention after a series of pulses, by in-situ Thermal Desorption Spectroscopy (TDS) in the irradiation chamber. The target heater will be used for this task and the released gas will be studied

with a quadrupole mass spectrometer (QMS). The suitability of OLMAT for dynamic hydrogen retention studies is supported by the fact that the energies and fluxes of the NBI fast particles are similar to those used in ion implantation on materials, including liquid lithium [25]. The OLMAT experiments will adequately mimic the ELMs impact on Sn, and SnLi surfaces. In the case of Li, due to the size of the target (i.e. the Li volume), the available particle fluxes in OLMAT will not be sufficient to obtain a relevant %H retention, or to reach the solubility limit required to produce LiH [11]. Therefore, loading of H_2 gas at medium-high temperatures [34] is deemed necessary to get closer to the expected conditions prevailing in colder areas near the divertor plate of DEMO. At high temperatures this procedure will lead to a fast hydride formation as reported elsewhere [18]. Then, the effect of large hydrogen content (few %) in lithium on the CPS resilience will be apparent, since it is expected that the refilling time and Li evaporation rate will be modified with respect to its clean state. Generated lithium hydrides will be used to study the effect of pore clogging in the CPS and its elimination by the incoming OLMAT particle flux.

The CW laser in Phase II will allow studying the role of ELMs in the reduction of surface lithium hydride formation and H retention in both Li and Sn. This effect should alleviate tritium retention issues in places where ELMs impact. Moreover, if the laser beam is expanded to simulate the strike point heat deposition as explained in section 2.3 then a new series of experiments may be performed. If the temperature at the simulated strike point is large enough for a sizable evaporation of lithium (or tin) to take place, then a slow flux will be generated to replenish the evaporated material. If the lateral replenishment on the CPS is fast enough the generated lithium hydride (and other dust impurities with tin, tungsten, etc.) may be drawn towards the strike point where it will be decomposed by the large temperatures there. This mechanism may be effective in reducing the total tritium retention and dust accumulation on the CPS surface.

3.3 Redeposition and dust

In DEMO LM divertor most of the evaporated and sputtered liquid metal atoms will undergo prompt redeposition. Values of >90% or even close to 99% are expected especially for lithium due to its easy ionization [11,20,35]. Even in a best-case scenario deposits will appear on surfaces with low or no ion flux like divertor cassettes and recessed areas of the first wall. Dust originating from tin deposits [14,33] may be a hazard in case of air or water ingress. Lithium deposits pose a higher risk due to its high reactivity, and its contribution to tritium in-vessel inventory when codepositing with tritium. However, these codeposits will only be relevant in cooled parts (usually at <500 K). Most of the main chamber and first wall will be at a temperature (usually >700 K) where most of the hydrogen isotopes are released, as experiments in PISCES-A have shown [36]. For lithium-tin alloys redeposition is the main possible showstopper [37,38]. Lithium will be preferentially sputtered and evaporated, close to 100% [38,39]. This could be beneficial in terms of plasma core contamination, but the change in composition may lead to the development of Li-rich high melting point (up to 1060 K) azeotropes, causing pore clogging, dust, etc.

Besides redeposition of LM divertor elements, contaminants from the main wall constitute an additional source of dust and precipitates on the CPS surface: mostly W, but also Fe and Cr from stainless steels will be present. Another source of impurities comes from residual air: oxides, nitrides, carbonates, etc. This is an issue especially for Li, as it reacts with any gas except noble gases. These dust and precipitates may lead to pore clogging and poor thermal behavior of the CPS.

OLMAT will be especially suited to study redeposition, compared to other divertor plasma simulator devices (especially in Phase III with long pulse operation). As can be seen in Figure 2, OLMAT beam has a Gaussian profile with a 1/e width of 20 cm. This will allow the beam to cover completely the target (initially of 10 cm diameter, but up to 25 cm in later phases), in an analogous way to DEMO divertor in the toroidal direction. The mean free path of a liquid metal atom at a pressure of 20 Pa (at maximum OLMAT beam power) is several mm, much lower than the beam and sample diameter. In this way, several cycles of erosion/redeposition must take place for a particle to escape from the plasma-irradiated area, very much as expected in the SOL surrounding the strike point in a DEMO divertor. This situation is different than in other linear plasma devices where a narrow (~ cm range) beam hits the LM sample. As the beam is usually smaller than the sample, then the evaporated and sputtered liquid metal atoms may react with the neutral gas surrounding the beam, leading to unrealistic H-rich co-deposit formation in the case of lithium and even in tin [33].

Dust and precipitates may be deposited/formed in the prechamber. Their effect on pore clogging and associated issues on the CPS may be studied along all OLMAT phases. Particularly in Phase II, deposit removal by ELMs and by the strike point may be simulated with the CW laser.

3.4 Vapor shielding

The interest in vapor shielding phenomena, described years ago in carbon-based materials, stems from their potential in redistributing the incoming power flux in a rather large volume by atomic processes and high radiation, strongly dumping the actual power reaching the material. Although the activity in vapor shielding research decayed as tungsten —the main plasma facing material for ITER— is unlikely to benefit from it due to its extremely low vapor pressure, a renewed interest has arisen in connection to liquid metals PFC concepts [40]. Experiments in MAGNUM linear plasma device have shown that vapor shielding is achieved at 1000-1200 K and 2000-2200 K for Li and Sn respectively [14]. It has been postulated that matching the external pressure by the LM vapor is required to trigger the vapor shielding effect [41]. This suggests that operation with vapor shielding is only possible with lithium, as Sn operating temperature would be too high. However, scaling up to DEMO is not a simple task. Vapor shielding is a complex process that depends not only on the incoming heat flux and the liquid metal properties, but may also evolve with the divertor pressure and magnetic field topology in front of the target (see for example [40]). At present, there is no consensus on the dominant physics mechanisms of the shielding effect.

OLMAT is especially suited to study vapor shielding physics thanks to the devoted chamber and associated diagnostics, both at the plasma side and at the target. The pressure generated by the NBI at the target is in the range of the estimated value for DEMO strike points, 10-20 Pa [31,32]. The temperature increase caused by OLMAT beam at maximum power, estimated to be in excess of 550 K (as explained in section 2.2), will allow the liquid lithium at a base temperature of 453 K to reach values where vapor shielding has been detected (1000-1200 K [14]). For tin reaching its vapor shielding temperature range (2000-2200 K [14]) will be more difficult, even considering the slower dissipation of the beam power in tin-based CPS which have a less favorable contact angle with the tungsten mesh. In any case, vapor shielding studies of tin are of limited interest due to the required operating temperature (2000-2200 K) at DEMO would be too high.

It should be noted that although the density of neutral particles in OLMAT is much lower ($P \sim 1/v_{beam}$) than in DEMO, making the mean free path of neutrals ejected by the LM ~100 times longer, the redeposition length is still in the order of millimeters if elastic collisions are dominant. Local plasma formation by fast particle collisions will be favored by the high rate of ions (2/3) in the sputtered lithium [42]. In this way, the lack of real divertor plasmas facing the target may be compensated, although no realistic assessment of the expected microscopic parameters is possible at this stage. In OLMAT the composition of such plasma will be dominated by the species belonging to the liquid metal, a situation quite different than that considered in LM target operation in DEMO, where target temperatures are restricted to keep impurity fluxes from the LM below 1% of the divertor plasma [1,2], in the range of 10^{24} m^{-2} s^{-1}. The OLMAT scenario offers the possibility to get insight into the situation of (accidentally) high temperature excursions of the LM divertor target.

3.5 Fatigue

Material failure by fatigue is an important issue of nuclear fusion reactors. There is still no feasible concept to work continuously for long periods of time (weeks/months) as present fossil fuel and fission reactors do. DEMO is actually prepared to work in 2 h pulses with a duty factor of 60-70% [1,43]. This means around 2850 pulses per year. During each pulse the reactor materials will ramp up (and down) fast from 400-500 K (heated by residual radiation and actively cooled) until an operational temperature of ~700 K at the first wall. A still wider temperature excursion is expected at the divertor. These cycles will impose very demanding forces on the materials, especially as most of them will be brittle due to the huge neutron irradiation: 1-9 dpa/year depending on material and location [1,43]. Due to fatigue, and surface erosion, first wall materials have an expected lifetime of about two years.

Although liquid metals obviously do not suffer fatigue, the solid material —tungsten— forming the CPS substrate does. Therefore, thermal fatigue on CPS substrate should be studied. Although fatigue-induced mechanical damage may be protected by the liquid metal, enhanced corrosion may still occur, especially with Sn. OLMAT pulses have a repetition rate of 2 minutes, or 200-250 pulses per day. Therefore the equivalent lifetime of DEMO divertor materials may be reproduced in 20-28 days. In this way during Phase I thermal fatigue may be studied, since even in these short pulses a temperature excursion of more than 550 K is expected in CPS targets, Figure 4. It is in Phase III, where thermal steady state is reached, when the more relevant results will be obtained, although the frequency of the pulses per day is still uncertain. Obviously, the exposure of more conventional divertor target solid materials, including the dry CPS may also be considered. The damage will be studied at CIEMAT Laboratory for nuclear fusion materials.

4. Summary

OLMAT, a new divertor plasma simulator has been presented. It is based on the upgrade of the existing NBI of stellarator (TJ-II), being the alternative operation of both devices possible. In this way the building and operational costs are greatly reduced. OLMAT will be specialized in liquid metal armor testing, aimed specially at CPS technology, which will make it unique in its kind.

The project has been divided in three phases. During Phase I the behavior of CPS samples under NBI pulses of 150 ms will be studied. In Phase II a CW laser will be used to simulate ELMs and strike points heat loads. And in Phase III wthe NBI source will be upgraded to generate multi-second pulses thereby achieving thermal steady state at the target.

A series of experiments has been sketched to study a wide range of CPS properties, some of them very specific to OLMAT as no other device is adequate for the study Among the general properties are: thermal and mechanical resilience of CPS against large heat and particle loads, including heat loads by ELMs; hydrogen retention in solution, hydrides formation and their effect on CPS properties; dust and precipitates effects; and refilling time studies. The specific properties are: reactor-relevant redeposition and codeposit formation due to the large beam; vapor shielding with an adjustable pressure; and material fatigue studies in viable timespan.

5. Acknowledgements

D. Alegre acknowledges the financial support from the fellowships “Ayuda para la Atracción del Talento Investigador de la Comunidad de Madrid”, ref. 2017-T2/AMB-5304 and Eurofusion Researcher Grant, TA ref AWP18-ERG-CIEMAT-Alegre.

This work has been supported by the Spanish Ministry of Science and Innovation (MINECO) with Project number RTI2018-096967-B-I00 and carried out within the framework of the EUROfusion Consortium and has received funding from the Euratom research and training program 2014-2018 and 2019-2020 under agreement No 633053. The views and opinions expressed herein do not necessarily reflect those of the European Commission.

Declarations

Funding: in acknowledgements

Conflicts of interest/Competing interests: in acknowledgements

Availability of data and material: not applicable

Code availability: Not applicable

6. Bibliography

1. R. Wenninger, R. Albanese, R. Ambrosino, F. Arbeiter, J. Aubert, C. Bachmann, L. Barbato, T. Barrett, M. Beckers, W. Biel, L. Boccaccini, D. Carralero, D. Coster, T. Eich, A. Fasoli, G. Federici, M. Firdaouss, J. Graves, J. Horacek, M. Kovari, S. Lanthaler, V. Loschiavo, C. Lowry, H. Lux, G. Maddaluno, F. Maviglia, R. Mitteau, R. Neu, D. Pfefferle, K. Schmid, M. Siccinio, B. Sieglin, C. Silva, A. Snicker, F. Subba, J. Varje, and H. Zohm, Nucl. Fusion **57**, 046002 (2017).

2. J. W. Coenen, S. Antusch, M. Aumann, W. Biel, J. Du, J. Engels, S. Heuer, A. Houben, T. Hoeschen, B. Jasper, F. Koch, J Linke, A. Litnovsky, Y. Mao, R. Neu, G. Pintsuk, J. Riesch, M. Rasinski, J. Reiser, M. Rieth, A. Terra, B. Unterberg, Th Weber, T. Wegener, J.-H. You, and C. Linsmeier, Phys. Scr. **2016**, 014002 (2016).
3. F. L. Tabarés, Plasma Phys. Control. Fusion **58**, 014014 (2016).
4. R. E. Nygren and F. L. Tabarés, Nuclear Materials and Energy **9**, 6 (2016).
5. T. W. Morgan, A. Vertkov, K. Bystrov, I. Lyublinski, J. W. Genuit, and G. Mazzitelli, Nuclear Materials and Energy **12**, 210 (2017).
6. Z. H. Wang, X. Jia, and M. J. Ni, Nucl. Fusion **58**, 126011 (2018).
7. D. N. Ruzic, W. Xu, D. Andruczyk, and M. A. Jaworski, Nucl. Fusion **51**, 102002 (2011).
8. D. N. Ruzic, M. Szott, C. Sandoval, M. Christenson, P. Fiflis, S. Hammouti, K. Kalathiparambil, I. Shchelkanov, D. Andruczyk, R. Stubbers, C. J. Foster, and B. Jurczyk, Nuclear Materials and Energy **12**, 1324 (2017).
9. J. S. Hu, G. Z. Zuo, R. Maingi, Z. Sun, K. Tritz, W. Xu, Q. X. Yang, D. Andruczyk, M. Huang, X. C. Meng, X. Z. Gong, D. N. Ruzic, M. J. Ni, B. N. Wan, and J. G. Li, Nuclear Materials and Energy **18**, 99 (2019).
10. X. Zhang and C. Pan, IEEE Transactions on Plasma Science **46**, 1539 (2018).
11. F. L. Tabarés, E. Oyarzabal, A. B. Martin-Rojo, D. Tafalla, A. de Castro, and A. Soleto, Nucl. Fusion **57**, 016029 (2017).
12. I. E. Lyublinski, A. V. Vertkov, and V. A. Evtikhin, Plasma Devices and Operations **17**, 265 (2009).
13. A. Vertkov, I. Lyublinski, M. Zharkov, G. Mazzitelli, M. L. Apicella, and M. Iafrati, Fusion Engineering and Design **117**, 130 (2017).
14. T. W. Morgan, P. Rindt, G. G. van Eden, V. Kvon, M. A. Jaworksi, and N. J. L. Cardozo, Plasma Phys. Control. Fusion **60**, 014025 (2018).
15. T. W. Morgan, D. C. M. van den Bekerom, and G. De Temmerman, Journal of Nuclear Materials **463**, 1256 (2015).
16. A. B. Martin-Rojo, E. Oyarzabal, T. W. Morgan, and F. L. Tabarés, Fusion Engineering and Design **117**, 222 (2017).
17. M. A. Jaworski, T. Abrams, J. P. Allain, M. G. Bell, R. E. Bell, A. Diallo, T. K. Gray, S. P. Gerhardt, R. Kaita, H. W. Kugel, B. P. LeBlanc, R. Maingi, A. G. McLean, J. Menard, R. Nygren, M. Ono, M. Podesta, A.L. Roquemore, S. A. Sabbagh, F. Scotti, C. H. Skinner, V. A. Soukhanovskii, D. P. Stotler, and the N. Team, Nucl. Fusion **53**, 083032 (2013).
18. E. Oyarzabal, A. B. Martín-Rojo, and F. L. Tabarés, Fusion Engineering and Design **117**, 217 (2017).
19. V. A. Evtikhin, I. E. Lyublinski, A. V. Vertkov, V. G. Belan, I. K. Konkashbaev, and L. B. Nikandrov, Journal of Nuclear Materials **271–272**, 396 (1999).
20. P. Rindt, T. W. Morgan, M. A. Jaworski, and N. J. L. Cardozo, Nucl. Fusion **58**, 104002 (2018).
21. A. J. Donné, J Fusion Energ **38**, 503 (2019).
22. *EUROfusion NEWSbrief Issue 27* (2020).
23. J. Guasp, M. Liniers, C. Fuentes, and G. Barrera, Fusion Technology **35**, 32 (1999).
24. M. Liniers, J. Damba, J. Guasp, J. A. Sebastián, F. Martín, B. Rojo, R. Carrasco, E. Sánchez, F. Miguel, G. Wolfers, A. Soleto, and E. Ascasíbar, Fusion Engineering and Design **123**, 259 (2017).
25. S. K. Erents, G. M. McCracken, and P. Goldsmith, J. Phys. D: Appl. Phys. **4**, 672 (1971).
26. C. Linsmeier, B. Unterberg, J. W. Coenen, R. P. Doerner, H. Greuner, A. Kreter, J. Linke, and H. Maier, Nucl. Fusion **57**, 092012 (2017).
27. A. V. Vertkov, I. E. Lyublinski, F. Tabares, and E. Ascasibar, Fusion Engineering and Design **87**, 1755 (2012).
28. X. Xu, N. Li, Z. Li, B. Chen, T. Y. Xia, T. Tang, B. Zhu, and V. Chan, Nucl. Fusion **59**, 126039 (2019).

29. S. J. Gee, R. Baldwin, A. Borthwick, D. Ciric, G. Crawford, L. Hackett, D. Homfray, D. Martin, J. Milnes, T. Mutters, M. Simmonds, R. Smith, R. Stephen, P. Stevenson, E. Surrey, C. Waldon, S. Warder, A. Whitehead, and D. Young, Fusion Engineering and Design **74**, 403 (2005).
30. M. Liniers, J. A. Quintana, B. Rojo, F. Martín-Díaz, F. Miguel, J. A. Sebastián, R. Carrasco, A. Soleto, E. Sánchez-Sarabia, A. Jiménez-Denche, C. Pastor, C. Rodríguez, J. Guasp, E. de la Cal, K. J. McCarthy, I. Pastor, and E. Ascasíbar, J. Inst. **14**, C09028 (2019).
31. V. Hauer and Chr. Day, *DEMO Exhaust Pumping Simulations for Different Divertor/Duct Configurations Enabling Plasma Operation* (Eurofusion, 2019).
32. S. Varoutis, F. Bonelli, Chr. Day, and Y. Igitkhanov, Nuclear Materials and Energy **12**, 668 (2017).
33. W. Ou, R. S. Al, J. W. M. Vernimmen, S. Brons, P. Rindt, and T. W. Morgan, Nucl. Fusion **60**, 026008 (2020).
34. E. Oyarzabal, A. B. Martin-Rojo, and F. L. Tabarés, Journal of Nuclear Materials **463**, 1173 (2015).
35. J. P. Allain and J. N. Brooks, Nucl. Fusion **51**, 023002 (2011).
36. F. L. Tabarés, D. Alegre, M. Baldwin, D. Nishijima, M. Simmonds, R. Doerner, E. Alves, and R. Mateus, Plasma Phys. Control. Fusion **59**, 044006 (2017).
37. C. J. Wen and R. A. Huggins, J. Electrochem. Soc. **128**, 1181 (1981).
38. F. L. Tabarés, E. Oyarzabal, A. B. Martin-Rojo, D. Tafalla, A. de Castro, F. Medina, M. A. Ochando, B. Zurro, and K. McCarthy, Nuclear Materials and Energy **12**, 1368 (2017).
39. M. Suchoňová, J. Krištof, M. Pribula, M. Veis, F. L. Tabarés, and P. Veis, Fusion Engineering and Design **117**, 175 (2017).
40. E. Marenkov and A. Pshenov, Nucl. Fusion **60**, 026011 (2020).
41. G. G. van Eden, T. W. Morgan, D. U. B. Aussems, M. A. van den Berg, K. Bystrov, and M. C. M. van de Sanden, Phys. Rev. Lett. **116**, 135002 (2016).
42. J. P. Allain, M. D. Coventry, and D. N. Ruzic, Phys. Rev. B **76**, 205434 (2007).
43. C. Bachmann, G. Aiello, R. Albanese, R. Ambrosino, F. Arbeiter, J. Aubert, L. Boccaccini, D. Carloni, G. Federici, U. Fischer, M. Kovari, A. Li Puma, A. Loving, I. Maione, M. Mattei, G. Mazzone, B. Meszaros, I. Palermo, P. Pereslavtsev, V. Riccardo, P. Sardain, N. Taylor, S. Villari, Z. Vizvary, A. Vaccaro, E. Visca, and R. Wenninger, Fusion Engineering and Design **98–99**, 1423 (2015).
, 1423 (2015).